Heat Conductance of the Quantum Hall Bulk

Ron Aharon Melcer[1,2], Avigail Gil[2], Vladimir Umansky[1,2], Moty Heiblum[1,2], Yuval Oreg[2],

Ady Stern[2], and Erez Berg[2]

[1] Braun Center for SubMicron Research, Department of Condensed Matter Physics,

  Weizmann Institute of Science, Rehovot, Israel, 76100

[2] Department of Condensed Matter Physics, Weizmann Institute of Science, Rehovot, Israel, 76100

The Quantum Hall Effect (QHE) is the prototypical realization of a topological state of matter. It emerges from a subtle interplay between topology, interactions, and disorder. The disorder enables the formation of localized states in the bulk that stabilize the quantum Hall states with respect to the magnetic field and carrier density. Still, the details of the localized states and their contribution to transport remain beyond the reach of most experimental techniques. Here, we describe an extensive study of the bulk's heat conductance. Using a novel 'multi-terminal' device, we separate the longitudinal thermal conductance (due to bulk's contribution) $\kappa_{\mathrm{xx}}T$ from the two-terminal value $\kappa_{\mathrm{2T}}T$, by eliminating the contribution of the edge modes. We find that when the field is tuned away from the conductance plateau center, the electronic states of the bulk conduct heat efficiently while the bulk remains electrically insulating. For fragile fractional states, such as the non-Abelian $\nu = 5/2$, we observe a finite $\kappa_{\mathrm{xx}}T$ throughout the plateau. We identify the localized states as the cause of the finite $\kappa_{\mathrm{xx}}T$ and propose a theoretical model which qualitatively explains our findings.

The magneto-conductance trace is the best-known signature of the quantum Hall effect (QHE). At integer (IQHE) or simple fractional (FQHE) values of the Landau-Levels (LL) fillings ν, the electrical conductance differs from the classical predictions. The transverse conductance exhibits plateaux (as a function of magnetic field or carrier density) with quantized values, $G_{\mathrm{xy}} = \nu G_0$ ($G_0 = \frac{e^2}{h}$), while the longitudinal conductance vanishes, $G_{\mathrm{xx}} \sim 0$. This observation implies that the bulk is insulating and current can only flow next to the sample's edge [1, 2]. Due to disorder, the localized states in the bulk get filled or emptied once the magnetic field is tuned away from the plateau's center. These localized states are a crucial ingredient for stabilizing the QHE states and a classical Hall conductance (i.e., without quantized plateaux

in G_{xy}) is expected to re-emerge in perfectly clean samples [3]. The contribution of the localized states to the electrical transport is negligible. Moreover, a deviation of the electrical conductance from its temperature-activated behavior, $G_{xx} \propto \exp\left(-\frac{\Delta}{T}\right)$, with Δ the energy gap and T the temperature, is hard to analyze quantitatively due to its smallness in the limit of $T \to 0$ [4, 5, 6].

The thermal Hall conductance is a second transport coefficient that is of great importance for studying the QHE. Similar to G_{xy}, the thermal Hall conductance is also quantized for QHE states[7, 8], $\kappa_{xy}T = \nu_Q \kappa_0 T$, where $\kappa_0 = \frac{\pi^2 k_b^2}{3h}$ is the thermal conductance quantum (T - temperature, k_b - Boltzman constant, h - Planck's constant coefficient), and ν_Q depends on the nature of the topological order. It is quantized to an integer for all Abelian states (integer and most fractional filling fractions) and a fraction for a non-Abelian state[9]. The value of ν_Q is a distinct property of the topological order of the bulk, which can provide crucial insight into the underlying ground state. The study of thermal transport in the QHE has accelerated in recent years, with experimental results manifesting the quantization of the *two-terminal* thermal conductance coefficient, $\kappa_{2T}T$ [10, 11, 12, 13]. These studies shed new light on the nature of fractional QHE states, especially of the exotic $\nu = 5/2$ state [11, 14]. However, the $\kappa_{2T}T$ is sensitive to the inter-mode thermal equilibration and a possible contribution of the bulk [15, 16, 17].

Following the fact that G_{xx} vanishes on the QHE plateaux, the contribution of the longitudinal thermal conductance, $\kappa_{xx}T$, was thus far neglected (despite some evidence of heat flow through the bulk[18, 19, 20]). The justification for such simplification arose due to the Wiedemann-Franz (WF) conjecture, which agreed experimentally in metallic systems with a fixed ratio $\kappa_{xx}/G_{xx} = \kappa_0/G_0 = L_0$, known as the 'Lorenz number'. Substantial violations of L_0 appeared in the limit $T \to 0$ in systems where a single electron picture is no longer valid, and the electronic transport is affected by interactions [21, 22, 23].

Recently we developed a novel technique that enables measuring local power [24], thus allowing a direct determination of the transverse thermal Hall conductance, $\kappa_{xy}T$. Here we employed this technique to determine also the heat flow through the bulk, using the term 'longitudinal thermal conductance' or $\kappa_{xx}T$. We found finite κ_{xx} at QHE conductance plateaux (where G_{xx}, $R_{xx}\sim0$), and propose a dominant heat transport mechanism.

The employed configuration, shown in Fig. 1, consists of a 'temperature source' (S) and a 'power meter' (PM) located downstream (see also Ref.[24] and Methods). A floating metallic source is heated by forcing two opposite-sign currents, I and $-I$, emanating from S_1 and S_2, leading to a zero source potential. The power is evacuated from the source via the outgoing gapless edge modes and possibly the bulk. Here, the edge modes flow to grounded contacts and do not reach the PM (see Fig. 1). This isolates the bulk's

contribution, as any excess power detected by the PM is strictly due to the bulk. The temperatures of S and PM are determined by measuring the emanating Johnson-Nyquist (JN) noise reaching the amplifiers' contacts, A_S and A_{PM}, respectively. The PM's elevated temperature is converted to the absorbed power using a separate calibration measurement (see Methods).

The longitudinal thermal conductance coefficient is extracted from the dissipated power in the PM and the temperature of the source,

$$P = N_\square \frac{\kappa_{xx}(T)}{2}(T_S^2 - T_0^2), \tag{1}$$

where T_S and T_0 are the source and the base temperatures (respectively), T their mean and $N_\square$ a geometric pre-factor (the *effective* number of squares, here being of the order of 1). The bulk's electrical conductance, G_{xx}, is measured by applying a voltage to the source contact and measuring the current drained through the PM contact (see Methods). In the rest of the manuscript, we simplify the expressions by absorbing the geometric pre-factor into the definition of κ_{xx} and G_{xx} (namely, taking $N_\square = 1$). We emphasize that the reported values of κ_{xx} are not universal (as they depend on the dimensions of the device), while the ratio κ_{xx}/G_{xx} is a general property of the bulk and thus independent of its geometry.

We start with filling factor $\nu = 2$. The power arriving at the PM is plotted as a function of the source's temperature at three different locations on the conductance plateau (Fig. 2a): (*i*) Center, $\nu = 2$ ($B = 6.4T$) - the first Landau level (both spins) is fully occupied; (*ii*) $\nu \sim 2.05$ ($B = 6.1T$) - localized states in the upper spinful LL2 are partly occupied; and (*iii*) $\nu \sim 1.95$ ($B = 6.7T$), localized quasi-holes in the spinful LL1 are partly occupied. We find a vanishingly small bulk heat conductance in the plateau's center, guaranteeing no 'parallel' mechanism that efficiently carries heat from S to PM (such as phonons or mobile carriers in the doping layer [25]). However, we observed a finite heat conductance when the field is tuned away from the plateau's center.

The thermal $\kappa_{xx}T$ and electrical G_{xx} conductances are plotted as a function of the magnetic field along the $\nu = 2$ plateau (Fig. 2b). We observe a narrow region of the magnetic field where κ_{xx} vanishes (near the center of the plateau). Towards the edge of the conductance plateau κ_{xx} increases rapidly, violating the WF relation by as much as two orders of magnitude, $\kappa_{xx}/G_{xx} \approx 200L_0$ for $B = 5.9T$.

The plotted temperature dependence of the transmitted power at three different fillings (Fig. 3a) suggests a temperature independent κ_{xx} in the range of 15–60mK. In addition, extending the temperature range of the source, $T_S = 20$– $100mK$ (thus creating large thermal gradients across the device) was also found to be consistent with temperature independent κ_{xx} (Fig. 3b). This implies that the thermal conductance, $\kappa_{xx}T \propto T$, in a similar fashion to metal at low temperatures [26].

We now discuss a simple physical picture that may explain the origin of the bulk thermal conductance in the QHE and its temperature dependence. In the presence of potential disorder, tuning the band filling away from the center of the conductance plateau adds localized quasi-particles (or quasi-holes). For a relatively smooth disorder potential (relative to the magnetic length), the added quasi-particles form incompressible "puddles" with fillings different from that of the bulk (see Fig. 4a). In the $\nu = 2$ bulk filling, added quasi-holes may form puddles with filling $\nu = 1$, with boundaries supporting gapless chiral edge modes. While particle tunneling between these puddles decays exponentially with the distance between the puddles, Coulomb interaction decays in a power law fashion. We assume that the puddles are large enough so that the level-spacing of excitations within a typical puddle is smaller than the temperature (we elaborate on this condition below). We find that the bulk is electrically insulating but thermally conducting under these conditions. This unique property could only be realized due to the topological nature of the QHE.

We make several simplifying assumptions to derive the thermal current's temperature dependence. First, we assume that the thermal conductance between the puddles is small enough to define a local temperature in each puddle. Second, the interaction region between two neighboring puddles is a segment of characteristic length L_{int} (around the point where they are closest), with interaction of a density-density form (illustrated in Fig. 4b). More details of the model, including the explicit form of the Hamiltonian and the derivation of the thermal conductance, are given in Supplementary Information (SI).

The low-energy excitations along the edge of each puddle are linearly dispersing chiral charge density waves (plasmons) that behave as free bosons. Under the assumptions above, the transmission coefficient $\mathcal{T}(\omega)$, defined as the probability of an incident excitation with frequency ω transmitted from one puddle to the next, given by[27] (see also SI),

$$\mathcal{T}(\omega) = \frac{\frac{u^2}{\tilde{v}^2}\sin^2\frac{\omega L_{int}}{\tilde{v}}}{1 + \frac{u^2}{\tilde{v}^2}\sin^2\frac{\omega L_{int}}{\tilde{v}}}. \tag{2}$$

Here u is the strength of the inter-edge interaction, and $\tilde{v} = \sqrt{v^2 - u^2}$ is the renormalized speed of excitations in the segment where the edges interact; and v is the speed of excitations along the puddle's edge away from the interaction region (for simplicity, v is taken to be the same in the two puddles). Notice that u is measured in velocity units and must satisfy $u < v$ (see SI). From this expression, the heat current flowing from the 'hot puddle' to the 'colder puddle' is,

$$J_Q(T_L, T_R) = v \int\limits_0^\infty \frac{dk}{2\pi} \hbar\omega_k \left[n_B\left(\frac{\hbar\omega_k}{k_b T_L}\right) - n_B\left(\frac{\hbar\omega_k}{k_b T_R}\right) \right] \mathcal{T}(\omega_k), \tag{3}$$

where T_L, T_R are the temperatures of the two puddles, $\omega_k = vk$ and $n_B(x)$ is the Bose function. In the limit $k_b T \gg \hbar v / L_{int}$, the thermal current simplifies to,

$$J_Q(T_L, T_R) = \tilde{\kappa}(T_L^2 - T_R^2), \tag{4}$$

where, for $u \ll v$, $\tilde{\kappa} = \frac{\kappa_0}{4}\frac{u^2}{\tilde{v}^2}$. In the opposite limit, $k_b T \ll \hbar v / L_{int}$, we find $J_Q \propto T^4$ [28, 29]. Taking $L_{int} \sim 1\mu$m and $v \sim 10^4$m/s, we obtain a characteristic temperature scale $T^\star = \frac{\hbar v}{k_b L_{int}} \sim 75$mK, of the order of the temperature in our experiments. Figure 4c depicts the thermal conductance between two puddles evaluated from Eq. 3. We find that the thermal conductance is approximately temperature independent for $T \gtrsim 0.1 T^\star$.

The model reproduces the temperature dependence of the thermal current observed experimentally. Despite its simplicity, the essential ingredients leading to our main conclusion (Eq. 4) are robust. Heat is transferred through the scattering of plasmon excitations by inter-edge interactions with a transmission coefficient, $\mathcal{T}(\omega)$. When averaged over an energy window of the order of the temperature, it is nearly temperature-independent since the oscillations of $\mathcal{T}(\omega)$ are averaged out, at a sufficiently high temperature. For v of the same order of magnitude as u, we obtain $\tilde{\kappa} \sim \kappa_0$. The actual value of κ_{xx}, probed in the experiment, is non-quantized and depends on the device geometry as well as the microscopic realization of the disorder which will fix $\tilde{\kappa}$.

The second Landau level hosts several more fragile fractional states [30, 31, 32], and among them we studied the $\nu = 7/3$ and the $\nu = 5/2$ states. The $\nu = 7/3$ state is believed to be a Laughlin fractional state on top of a full spinless first Landau level[33]. The $\nu = 5/2$ is the only (well-developed) even-denominator state [34]. Its underlying order in the bulk has been the center of intensive experimental and theoretical study in the past two decades[35]. The most decisive identification comes from thermal transport experiments [11, 14], which support a topological order known as Particle-Hole Pfaffian (PH-Pf)[36]. The PH-Pf ground state is inconsistent with current numerical simulations supporting a different non-Abelian order [37, 38].

Our device exhibits Hall resistance plateaus at $\nu = 7/3$ and $\nu = 5/2$ (Fig. 5a), with a vanishingly small bulk conductance at the center of the conductance plateau (as low as $G_{xx} \sim 5 \times 10^{-3} G_0$). On the other hand, the bulk's thermal conductance coefficient, κ_{xx}, remains finite throughout the plateau; never below $\kappa_{xx} = 0.3\kappa_0$ (a two-orders-of-magnitude violation of the WF relation, see Figs. 5b & 5c). We attribute this observation to the small energy gap of these states, leading to excited quasi-particles (and

quasi-holes), even at the plateau's center. In longer devices (hundreds of microns in length) fabricated on similar-quality GaAs, the expected values of the two-terminal thermal conductance were measured (for example. $\kappa_{2T} = 3\kappa_0$ for $\nu = 7/3$) [11, 14]. This implies that the quantized heat flowed next to the sample's edge with a negligible bulk contribution. The mechanism which governs the dependence of κ_{2T} on the device geometry is still not understood and requires further research in dedicated devices.

Very little is known about the properties of the localized states in the electrically insulating 2D bulk of topologically non-trivial materials. Studying the heat flow through the bulk [20] of QHE states, we find a substantial heat conductance in the integer and fractional QHE states (in particular away from the center of the conductance plateaux) and attribute it to interacting circulating currents around incompressible, disorder-induced, puddles. Deviating further from the center of the conductance plateau increases the heat flow, which we associate with the increased number and size of the puddles. Moreover, we find that the longitudinal thermal conductance coefficient κ_{xx} (through the bulk) is temperature independent in the measured temperature range (15-100mK). Bulk thermal conductance is an essential ingredient in thermal conductance studies. A deeper understanding is required to determine its effect on topological thermal Hall conductance (κ_{xy}).

Methods

Sample preparation

The mesa is etch-defined, formed by optical lithography and wet-etching (using the solution $H_2O: H_2O_2: H_2PO_4$ - 50:1:1). The narrow etched lines were separately patterned using e-beam lithography and etched by reactive-ion-etching (RIE) using BCl_3/Ar gases. The Ohmic contacts and the gates were patterned using the standard e-beam-liftoff technique. The ohmic contacts consist of (from GaAs surface upwards) Ni(7nm), Au(250nm), Ge(125nm), Ni (82nm), Au (10nm), alloyed at $440^\circ C$ for 80 seconds. After preparing the contacts, the sample was covered with 25nm of HfO_2 deposited at $200^\circ C$ using ALD. The gates consist of 5nm Ti and 15nm Au.

The device has three different gate patterns: (***i***) Thin gates (appear in gray in Fig. 1) that enable local depletion of the carriers. Once activated, they can force the edge modes to flow from S to PM. These gates were grounded throughout the measurements, guaranteeing that the edge modes flow to the ground. (***ii***) Global gates that cover the regions to the left of S and the right of the PM (yellow color in Fig. 1). These gates are used to induce a $\nu = 2$ filling factor in these regions. Note that the measured transport only occurs in the un-gated region between S and PM. The gated regions support Sources' DC currents and Johnson-Nyquist noise. The integer filling offers simplifications to the process of calibration of amplification gain and T_0 (see Supplementary information). (***iii***) Grounded gates that cover S and PM contacts (the leads grounding these gates appear in gray in Fig. 1). The 'ohmic contact-oxide-gate' forms a capacitor ($c{\sim}0.5pF$). The enhanced capacitance ensures that the contacts behave as ideal metallic reservoirs[39].

The HfO_2 is etched from the bonding pads using RIE (BCl_3/Ar gases).

Probing κ_{xx} and G_{xx}

The longitudinal electrical conductivity, σ_{xx}, and thermal conductivity, $k_{xx}T$, are specific transport properties of the bulk. These properties are usually measured indirectly, using probes placed along the sample's edge (for example, in a Hall-bar geometry). Such methodology allows measuring the global electrical (G_{xx}), and thermal ($\kappa_{xx}T$) conductances. For 2D materials, the specific and the global coefficients are equal, up to a device-specific geometric factor known as the number of squares, $N_\square$. Namely,

$$\sigma_{xx} = G_{xx}/N_\square,$$
$$k_{xx} = \kappa_{xx}/N_\square. \qquad \text{(M1)}$$

Thus the conductance is usually reported per square. Here we adopted a different approach (described in detail in the main text and the sections below), which is conceptually more suitable for measuring the longitudinal thermal conductance in QHE states. The main problem of measuring the temperature drop along an edge segment (for example, in a Hall-bar geometry) is that it can be sensitive to the thermal conductivity of the bulk (which we want to probe) as well as properties of the edge modes themselves, mostly thermal equilibration (when counter-propagating modes are present)[15, 40, 41], and dissipation of heat from the edge to the environment[41, 42]. We overcame these complications by grounding the edge modes and measuring the heat flow through the bulk directly.

A possible drawback of our technique is that we are unable to determine the geometric factor precisely, $N_\square$ (which is of order one). Thus, the values of κ_{xx} reported in the main text are equal to the longitudinal conductivity up to a multiplying pre-factor (of order unity). Crucially, we measured the longitudinal electrical conductance using the same contacts as for the thermal conductance (S and PM). Using the same geometry guarantees that the observed WF ratio of the thermal and electrical conductances is purely a bulk property. Moreover, it allows us to rule out the possibility that the observed violations of the WF relation are simply an artifact caused by a 'dirty' region or some density inhomogeneity.

Electrical conductance measurements

We use a low-frequency signal (11–17Hz) with a lock-in technique for conductance measurements. We source current I_S from S_1 to the source contact, which causes the voltage of the source to be,

$$V = \frac{I_S}{G_{S \to G}},\tag{M2}$$

with $G_{S \to G}$ the overall conductance from the source to the ground. To measure the longitudinal conductance, we need to measure the current that flows through the bulk, $G_{xx} = I/V$. We probe the source-to-PM current, I, via the measurement of the PM voltage (in a contact located in one of the regions to the right of the PM),

$$I = V_{PM}\, G_{PM \to G},\tag{M3}$$

with $G_{PM \to G}$ the conductance from the PM to the ground. This allows us to extract the longitudinal conductance,

$$G_{xx} = \frac{I}{V} = \frac{V_{PM}}{I_S} G_{S \to G} G_{PM \to G}.\tag{M4}$$

Relying on the fact that $G_{xy} \gg G_{xx}$, we consider only the contribution of the edge modes to the electrical conductance $G_{S \to G}$ and $G_{PM \to G}$. For example, when all the regions are at $\nu = 2$, the conductance from either the PM or the Source to ground is simply the number of mesas connected to the contact time the quantized conductance,

$$G_{S \to G} = G_{PM \to G} = 3 \times \frac{2e^2}{h},\tag{M5}$$

leading to the conductance according to,

$$G_{xx} = 36 \left(\frac{e^2}{h}\right)^2 \frac{V_{PM}}{I_S}.\tag{M6}$$

Thermal conductance measurements

Probing the longitudinal thermal conductance requires measuring the power impinging upon the PM as a function of the source's temperature. We accomplish this measurement in two steps: (*i*) We heat the Source contact using two opposite polarity DC currents and measure the temperature of the PM, T_{PM}, as a function of the temperature of the source T_S. (*ii*) We calibrate the PM by measuring its temperature

T_{PM} against a known heating power P_{cal}. We accomplish this by dissipating a known power using opposite sign currents I_{cal} and $-I_{\text{cal}}$ sourced from contacts S_1^{cal} and S_2^{cal} (in Fig. 1) respectively. This causes the direct dissipation of power $P_{\text{cal}} = I_{\text{cal}}^2/G_{\text{xy}}$ on the PM (here, the source contact remains cold). The measurement of T_{PM} against P_{cal} manifests the power-meter calibration.

Combining the primary measurement with the calibration enables us to determine the impinging power on the PM as a function of T_S (see SI for further discussion). We acquire κ_{xx} by linear fitting the power against T_S^2, according to Eq. 1.

Once we established that κ_{xx} is temperature independent, we were able to improve the efficiency of our measurement by measuring the power only for a single source temperature T_S (instead of scanning and fitting, which requires significantly longer averaging time). This method was applied for the measurement of $\nu = 5/2$ (Fig. 5c) with $T_S = 40\text{mK}$ (we performed a full scan only in the center of the plateau); for $\nu = 3$, with $T_S = 50\text{mK}$; and for $\nu = 4/3$ (see SI).

Acknowledgments

Author contribution

R.A.M designed the experiment, fabricated the devices, performed the measurements and analyzed the data. M.H supervised the experiment's design, execution and the data analysis. A.G, E.B, Y.O and A.S developed the theoretical model. V.U grew the GaAs heterostructures. All authors contributed to the writing of the manuscript.
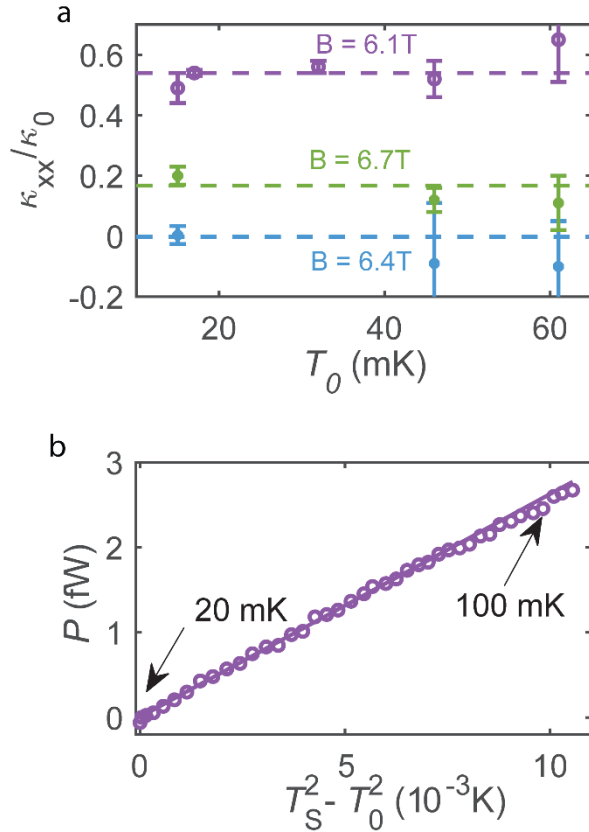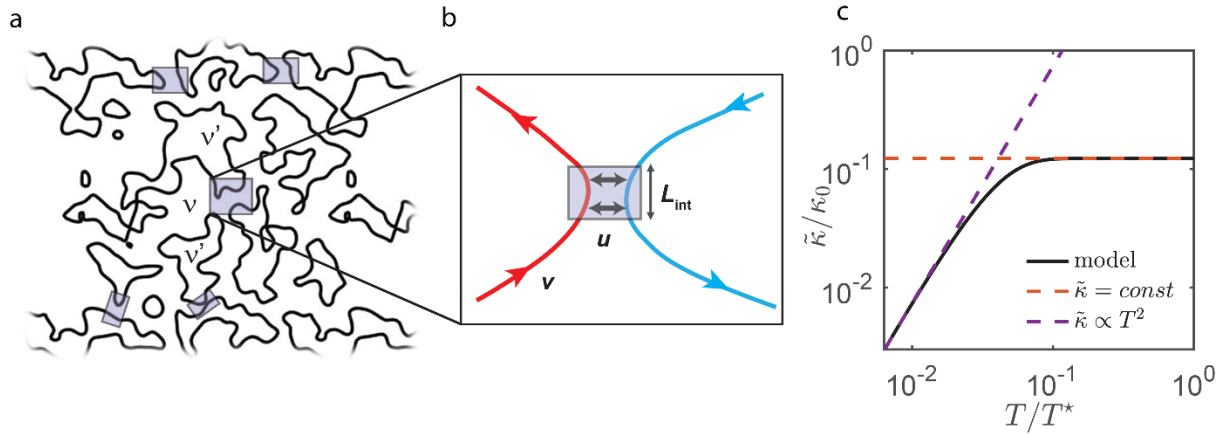
Figures
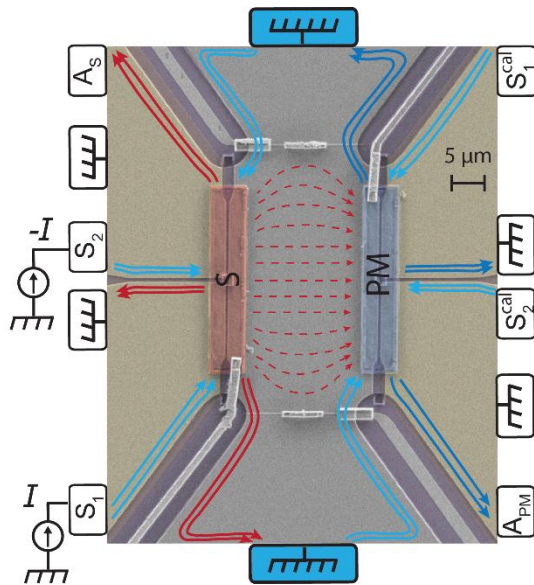
Figure 1 – The measured device. A false-colored SEM image of the device's heart - was used to measure the longitudinal thermal conductance. The mesa is divided into several regions by narrowly etched areas (purple). Transport is carried in the central region between the source contact (S, colored red) and the power-meter contact (PM, colored dark blue). In the experiment, we heat the source contact by sourcing currents $I, -I$ from S_1 and S_2, respectively. The edge modes (solid lines) that leave S flow to the ground, allowing heat transfer from S to the PM only via the bulk (narrow dashed red lines). The energy currents from S increase the PM temperature. Both temperatures, T_{PM} and T_S, are probed simultaneously by measuring the Johnson-Nyquist noise in A_{PM} and A_S, respectively. The temperature of the PM is converted to the impinging power using a calibration measurement (see Methods). The regions to the left of S and the right of the PM (used for noise measurement and control) are fully covered with top gates that tune the regions to $\nu = 2$ (faint yellow). The integer filling eases the calibration of temperature and power (see SI).
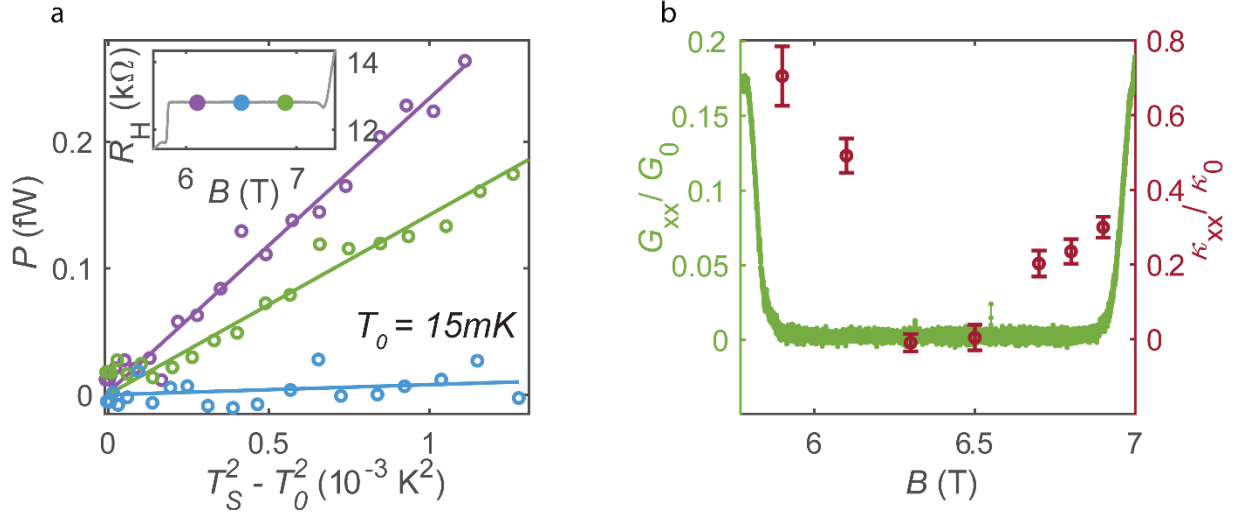
Figure 2 – Longitudinal thermal conductance in filling factor $\nu = 2$ at $T_0 = 15\text{mK}$. (a) Impinging power at the power meter (PM) as a function of the source (S) temperature at three values of the magnetic field on the $\nu = 2$ plateau: Blue – center; purple – particle side; green – hole side (see inset). Away from the center, finite heat flows from S to PM (through the bulk of the sample). By linear fitting the PM power as a function of temperature squared (straight colored lines), κ_{xx} is extracted (Eq. 1). **(b)** Longitudinal electrical and thermal conductance on the $\nu = 2$ plateau. The longitudinal conductance, G_{xx}, vanishes throughout the plateau (green). The thermal conductance κ_{xx}, extracted from the linear fits in **(a)**, is finite away from the plateau's center.

Figure 3 – Temperature dependence of κ_{xx}. (a) The longitudinal thermal conductance measured as a function of base temperature, T_0 extracted by linear fitting the impinging power at the PM as a function of source temperature squared (see SI). κ_{xx} appears to be temperature independent for a few magnetic field values on the plateau (see Fig. 2b). **(b)** Power impinging on the power-meter (PM) as a function of the source (S) temperature for a large temperature range, $19 - 100$mK. The fitted line to the data remains linear up to $T_S = 80$mK.

Figure 4 – Illustration of the model used for the thermal current. (a) Density puddles at filling factor v' inside a bulk state at filling factor v, formed in the presence of smooth disorder when the magnetic field is away from the center of the v plateau. Chiral edge modes circulate at the boundaries of the puddles. **(b)** Diagram of the puddle-puddle interaction: The distance between two neighboring puddles is large enough to suppress inter-puddle electron tunneling but small enough to allow significant Coulomb interactions. The interactions are of constant strength u and take place in a finite region with a characteristic length of L_{int} (where the edges are the closest). The velocity of the excitations away from the interacting region, v, is assumed to be constant and equal in the interacting puddles. **(c)** Thermal conductance between two interacting puddles. The right puddle is at temperature T, and the left is at temperature $T + dt$ (with $dt \ll T$). The thermal conductance coefficient between the puddles is calculated as $\tilde{\kappa} = J_Q/2k_bT dt$, with J_Q according to Eq. 3. For $T \sim 0.1T^\star$ ($T^\star = \hbar/vk_bL_{in} \approx 75$mK), $\tilde{\kappa}$ saturates and becomes temperature independent, in agreement with the experimental observations. Here we take $u/v = 0.1$.
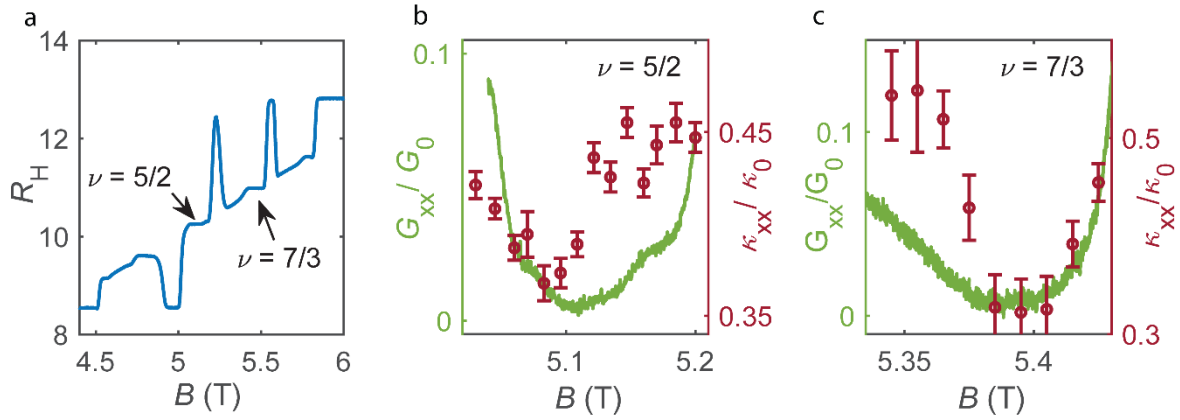
Figure 5 – Thermal conductance of the bulk at fillings $\nu = 7/3$ and $\nu = 5/2$. (a) The transverse Hall resistance as a function of the magnetic field manifests plateaus at fractional filling factors in the range between $\nu = 2$ and $\nu = 3$. **(b, c)** G_{xx} (green) and κ_{xx} (red) as a function of the magnetic field along the $\nu = 5/2$ **(b)** and $\nu = 7/3$ **(c)** plateaus. Close to the center of each plateau, G_{xx} is vanishingly small, yet, κ_{xx} remains finite.

References:

1. Laughlin RB. Quantized Hall Conductivity in 2 Dimensions. *Physical Review B* 1981, **23**(10)**:** 5632-5633.

2. Halperin BI. Quantized Hall conductance, current-carrying edge states, and the existence of extended states in a two-dimensional disordered potential. *Physical Review B* 1982, **25**(4)**:** 2185-2190.

3. Girvin SMaP, R. *The quantum Hall effect*. Springer-Verlag, 1987.

4. Tsui DC, Störmer HL, Gossard AC. Zero-resistance state of two-dimensional electrons in a quantizing magnetic field. *Physical Review B* 1982, **25**(2)**:** 1405-1407.

5. Boebinger GS, Stormer HL, Tsui DC, Chang AM, Hwang JCM, Cho AY*, et al.* Activation energies and localization in the fractional quantum Hall effect. *Physical Review B* 1987, **36**(15)**:** 7919-7929.

6. Boebinger GS, Chang AM, Stormer HL, Tsui DC. Magnetic Field Dependence of Activation Energies in the Fractional Quantum Hall Effect. *Physical Review Letters* 1985, **55**(15)**:** 1606-1609.

7. Kane CL, Fisher MPA. Quantized thermal transport in the fractional quantum Hall effect. *Physical Review B* 1997, **55**(23)**:** 15832-15837.

8. Cappelli A, Huerta M, Zemba GR. Thermal transport in chiral conformal theories and hierarchical quantum Hall states. *Nuclear Physics B* 2002, **636**(3)**:** 568-582.

9. Read N, Green D. Paired states of fermions in two dimensions with breaking of parity and time-reversal symmetries and the fractional quantum Hall effect. *Physical Review B* 2000, **61**(15)**:** 10267-10297.

10. Jezouin S, Parmentier FD, Anthore A, Gennser U, Cavanna A, Jin Y*, et al.* Quantum Limit of Heat Flow Across a Single Electronic Channel. *Science* 2013, **342**(6158)**:** 601-604.

11. Banerjee M, Heiblum M, Umansky V, Feldman DE, Oreg Y, Stern A. Observation of half-integer thermal Hall conductance. *Nature* 2018, **559**(7713)**:** 205-210.

12. Banerjee M, Heiblum M, Rosenblatt A, Oreg Y, Feldman DE, Stern A*, et al.* Observed quantization of anyonic heat flow. *Nature* 2017, **545**(7652)**:** 75-79.

13. Srivastav SK, Sahu MR, Watanabe K, Taniguchi T, Banerjee S, Das A. Universal quantized thermal conductance in graphene. *Science Advances* 2019, **5**(7)**:** eaaw5798.

14. Dutta B, Umansky V, Banerjee M, Heiblum M. Isolated ballistic non-abelian interface channel. *Science* 2022, **377**(6611)**:** 1198-1201.

15. Melcer RA, Dutta B, Spånslätt C, Park J, Mirlin AD, Umansky V. Absent thermal equilibration on fractional quantum Hall edges over macroscopic scale. *Nature Communications* 2022, **13**(1)**:** 376.

16. Srivastav SK, Kumar R, Spånslätt C, Watanabe K, Taniguchi T, Mirlin AD*, et al.* Vanishing Thermal Equilibration for Hole-Conjugate Fractional Quantum Hall States in Graphene. *Physical Review Letters* 2021, **126**(21)**:** 216803.

17. Srivastav SK, Kumar R, Spånslätt C, Watanabe K, Taniguchi T, Mirlin AD*, et al.* Determination of topological edge quantum numbers of fractional quantum Hall phases by thermal conductance measurements. *Nature Communications* 2022, **13**(1)**:** 5185.

18. Altimiras C, le Sueur H, Gennser U, Anthore A, Cavanna A, Mailly D*, et al.* Chargeless Heat Transport in the Fractional Quantum Hall Regime. *Physical Review Letters* 2012, **109**(2).

19. Venkatachalam V, Hart S, Pfeiffer L, West K, Yacoby A. Local thermometry of neutral modes on the quantum Hall edge. *Nature Physics* 2012, **8**(9)**:** 676-681.

20. Inoue H, Grivnin A, Ronen Y, Heiblum M, Umansky V, Mahalu D. Proliferation of neutral modes in fractional quantum Hall states. *Nature Communications* 2014, **5:** 4067.

21. Tanatar MA, Paglione J, Petrovic C, Taillefer L. Anisotropic Violation of the Wiedemann-Franz Law at a Quantum Critical Point. *Science* 2007, **316**(5829)**:** 1320-1322.

22. Wakeham N, Bangura AF, Xu X, Mercure J-F, Greenblatt M, Hussey NE. Gross violation of the Wiedemann–Franz law in a quasi-one-dimensional conductor. *Nature Communications* 2011, **2**(1)**:** 396.

23. Crossno J, Shi JK, Wang K, Liu X, Harzheim A, Lucas A*, et al.* Observation of the Dirac fluid and the breakdown of the Wiedemann-Franz law in graphene. *Science* 2016, **351**(6277)**:** 1058-1061.

24. Melcer RA, Konyzheva S, Heiblum M, Umansky V. Direct determination of the topological thermal conductance via local power measurement. *Nature Physics* 2023.

25. Sammon M, Banerjee M, Shklovskii BI. Giant violation of Wiedemann-Franz law in doping layers of modern AlGaAs heterostructures. 2019. p. arXiv:1904.04758.

26. Lifshitz EM, Pitaevskii LP. *Physical Kinetics: Volume 10*. Elsevier Science, 1995.

27. Oreg Y, Finkel'stein AM. Interedge Interaction in the Quantum Hall Effect. *Physical Review Letters* 1995, **74**(18)**:** 3668-3671.

28. Gutman DB, Protopopov IV, Burin AL, Gornyi IV, Santos RA, Mirlin AD. Energy transport in the Anderson insulator. *Physical Review B* 2016, **93**(24)**:** 245427.

29. Aita H, Arrachea L, Naón C, Fradkin E. Heat transport through quantum Hall edge states: Tunneling versus capacitive coupling to reservoirs. *Physical Review B* 2013, **88**(8)**:** 085122.

30. Pan W, Xia JS, Shvarts V, Adams DE, Stormer HL, Tsui DC*, et al.* Exact Quantization of the Even-Denominator Fractional Quantum Hall State at v=5/2 Landau Level Filling Factor. *Physical Review Letters* 1999, **83**(17)**:** 3530-3533.

31. Pan W, Xia JS, Stormer HL, Tsui DC, Vicente C, Adams ED*, et al.* Experimental studies of the fractional quantum Hall effect in the first excited Landau level. *Physical Review B* 2008, **77**(7).

32. Kumar A, Csáthy GA, Manfra MJ, Pfeiffer LN, West KW. Nonconventional Odd-Denominator Fractional Quantum Hall States in the Second Landau Level. *Physical Review Letters* 2010, **105**(24)**:** 246808.

33. Balram AC, Jain JK, Barkeshli M. ${\mathbb{Z}}_{n}$ superconductivity of composite bosons and the $7/3$ fractional quantum Hall effect. *Physical Review Research* 2020, **2**(1)**:** 013349.

34. Halperin BI and Jain JK. *Fractional Quantum Hall Effects*, 2020.

35.   Ma KKW, Peterson MR, Scarola VW, Yang K. Fractional quantum Hall effect at the filling factor v=5/2. 2022. p. arXiv:2208.07908.

36.   Son DT. Is the composite fermion a Dirac particle? *Physical Review X* 2015, **5**(3)**:** 031027.

37.   Zaletel MP, Mong RSK, Pollmann F, Rezayi EH. Infinite density matrix renormalization group for multicomponent quantum Hall systems. *Physical Review B* 2015, **91**(4)**:** 12.

38.   Rezayi EH. Landau Level mixing and the ground state of the *v*=5/2 quantum Hall effect. *Physical Review Letters* 2017, **119**(2)**:** 026801.

39.   Sivre E, Anthore A, Parmentier FD, Cavanna A, Gennser U, Ouerghi A*, et al.* Heat Coulomb blockade of one ballistic channel. *Nature Physics* 2018, **14**(2)**:** 145-148.

40.   Park J, Mirlin AD, Rosenow B, Gefen Y. Noise on complex quantum Hall edges: Chiral anomaly and heat diffusion. *Physical Review B* 2019, **99**(16)**:** 161302.

41.   Aharon-Steinberg A, Oreg Y, Stern A. Phenomenological theory of heat transport in the fractional quantum Hall effect. *Physical Review B* 2019, **99**(4)**:** 6.

42.   Rosenblatt A, Konyzheva S, Lafont F, Schiller N, Park J, Snizhko K*, et al.* Energy Relaxation in Edge Modes in the Quantum Hall Effect. *Physical Review Letters* 2020, **125**(25)**:** 256803.

Supplementary Information for: Heat Conductance of the Quantum Hall Bulk

Ron Aharon Melcer[1,2], Avigail Gil[2], Vladimir Umansky[1,2], Moty Heiblum[1,2], Yuval Oreg[2],

Ady Stern[2], and Erez Berg[2]

[1] Braun Center for SubMicron Research, Department of Condensed Matter Physics,

  Weizmann Institute of Science, Rehovot, Israel, 76100

[2] Department of Condensed Matter Physics, Weizmann Institute of Science, Rehovot, Israel, 76100

Microscopic model for the heat transport

To calculate the heat current between two thermalized puddles in the bulk, we need to find the energy transfer rate of excitations from one chiral edge state to the other. This requires calculating the transmission amplitude of excitations due to inter-edge interactions, which was derived in Ref. 30. For completeness, we provide the derivation here.

The bosonized Hamiltonian that describes the system of two quantum hall edge states (R and L, see Fig. 4b) interacting through density-density interactions is given by:

$$H = \int dx \frac{v}{4\pi} [(\partial_x \phi_R)^2 + (\partial_x \phi_L)^2] + \frac{u(x)}{2\pi} \partial_x \phi_R \partial_x \phi_L. \tag{S1}$$

For simplicity, we treat the case of integer quantum Hall states, although a similar treatment applies for many fractional states as well. In the integer case, the fields ϕ_R, ϕ_L satisfy the commutation relations:

$$[\phi_R(x), \partial_x \phi_R(x')] = 2\pi i \delta(x - x'),$$
$$[\phi_L(x), \partial_x \phi_L(x')] = -2\pi i \delta(x - x'). \tag{S2}$$

In our model, the inter-edge interaction potential $u(x)$ is taken to be a constant over a finite region of length L_{int} where the puddles are closest to each other, and zero away from this region:

$$u(x) = \begin{cases} u, & 0 < x < L_{int} \\ 0, & \text{otherwise.} \end{cases} \tag{S3}$$

The equation of motion is given by:

$$\partial_t \phi_n(x, t) = i[H, \phi_n] = \pm[v \partial_x \phi_n + u(x) \partial_x \phi_{\bar{n}}], \tag{S4}$$

Where $n = R$ or L, $\bar{n}$ is the chirality opposite to n, and $\pm$ refers to R or L. Far away from the interaction region, the velocity of the edge modes is given by v, whereas in the interacting region, the renormalized velocity is given by $\tilde{v} = \sqrt{v^2 - u^2}$.

By imposing matching boundary conditions for plane wave excitations incoming from one of the edge modes, we find the reflection amplitude, defined as the amplitude of an excitation exiting the interacting region in the same edge state:

$$r(\omega) = \frac{\left(1 + \frac{\tilde{v} - v}{\tilde{v} + v}\right) e^{i\left(\frac{\omega}{\tilde{v}} - \frac{\omega}{v}\right)L_{int}}}{1 + \frac{\tilde{v} - v}{\tilde{v} + v} e^{2i\frac{\omega}{\tilde{v}}L_{int}}}. \tag{S5}$$

Squaring the reflection amplitude to obtain the transmission coefficient of excitations from one edge state to the other:

$$\mathcal{T}(\omega) = 1 - |r(\omega)|^2 = \frac{\frac{u^2}{\tilde{v}^2} \sin^2\left(\frac{\omega}{\tilde{v}} L_{int}\right)}{1 + \frac{u^2}{\tilde{v}^2} \sin^2\left(\frac{\omega}{\tilde{v}} L_{int}\right)} \tag{S6}$$

Assuming that the incoming excitations are thermalized, the thermal current is given by Eq. 3.

Methodology

In this section, we wish to describe in detail the method we employed in order to measure the longitudinal thermal conductance in the quantum Hall Effect (QHE) regime. In order to exemplify our technique, we will accompany this section with a step-by-step analysis of the raw data.

Noise measurement

In the experiment, we heat up the source (S) by sourcing opposite sign currents I, $-I$ from contacts S_1 and S_2 respectively. This causes the dissipation of power $P_S = \frac{I^2}{G_{xy}}$, while keeping the source potential zero. The dissipated power on the source causes its temperature T_S to increase. All the edge modes leaving the source flow to the ground, but in the presence of non-zero longitudinal thermal conductance, heat can propagate through the bulk and cause an increase to the power-meter's temperature, T_{PM}. We simultaneously measure the temperature of the source and the power-meter (PM). This is accomplished by the measurement of the excess current noise in amplifiers' contacts located downstream to the source and the PM (contacts A_S, and A_{PM} respectively in Fig. 1 of the main text). The raw noise data for $\nu = 2.05$ ($B = 6.1T$) is plotted in Fig. S1a. The excess current fluctuations are proportional to the temperature of the contact from which the edge emanates (due to the conservation of current). The low-frequency power spectral density of the noise arriving to A_S is given by[1]

$$S_I = 2k_b G^\star (T_S - T_0). \tag{S7}$$

Here, k_b is the Boltzmann constant, T_0 is the base temperature and $G^\star$ is the effective conductance for noise measurement,

$$G^\star = \frac{G_{S\to A}G_{S\to G}}{G_{S\to A} + G_{S\to G}}, \tag{S8}$$

With $G_{S\to A}$ ($G_{S\to G}$) is the conductance from the source to the amplifier (ground). In the measurement of all the states ($\nu = 2, \nu = 7/3$ and $\nu = 5/2$) the region connecting the source to A_S (as well as the region connecting the PM to A_{PM}) was tuned to $\nu = 2$ using a top gate. Thus, we had $G^\star = \frac{4}{3}\frac{e^2}{h}, \frac{26}{19}\frac{e^2}{h}$, and $\frac{18}{13}\frac{e^2}{h}$, for $\nu = 2, \nu = 7/3$, and $\nu = 5/2$ respectievely. Eq. S7 (and the equivalent formula for the PM) is used to extract T_S and T_{PM} from the measured noise (Fig. S1b).

Power-meter calibration

The second step of the measurement is to convert the temperature of the PM to impinging power. This is accomplished by a separate calibration measurement. Here, the source contact is not heated. Instead, we dissipate power directly on the PM contact, by sourcing two opposite currents, I_{cal}, and $-I_{cal}$ from S_1^{cal} and S_2^{cal} (in Fig. 1 of the main text), respectively (Fig. S1c). This allows measuring T_{PM} against a known power,

$$P_{cal} = \frac{I_{cal}^2}{G_{xy}}, \tag{S9}$$

(Fig. S1d). Finally, we use the power calibration to convert T_{PM} to impinging power, which could be plotted as a function of the heater temperature (Fig. S1e), and allows the extraction of κ_{xx}.

Additional QHE states

In addition to the data presented in the main text, we measured the longitudinal thermal conductance of other integer and fractional QHE states. For all the measured states, we were able to detect finite conductance of heat through the bulk. Here, in order to efficiently measure κ_{xx} for many values of magnetic field, we did not scan the source temperature. Instead, we relied on κ_{xx} being temperature independent and measured for a constant $T_S = 50\text{mK}$. Extracting the longitudinal thermal conductance according to,

$$\kappa_{xx} = 2\frac{P}{T_S^2 - T_0^2}. \tag{S10}$$

We ensure the applicability of this efficient method by the fact that the value of κ_{xx} agrees between the two methods (when measured for the same magnetic field).

Integer QHE $\nu = 3$

The behavior of this integer state resembles $\nu = 2$ (Fig. S2a). At the center of the plateau κ_{xx} vanishes, and it increases as the magnetic field is tuned away from the center. Here, unlike $\nu = 2$, the value of κ_{xx} appears to increase symmetrically in the 'particle' and the 'hole' sides of the plateau.

Fractional QHE $\nu = 4/3$

The $\nu = 4/3$ is a robust fractional state in the first Landau level (LL). The spin-up LL is completely full and the spin-down LL is one third full, forming a Laughlin state. Here, similar to the integer fillings, we observe vanishing κ_{xx} near the center of the plateau. κ_{xx} increases as the field is tuned away (Fig. S2b). Interestingly, for this fractional state, the region where $\kappa_{xx}{\sim}0$ is shifted slightly from the center of the $G_{xx}{\sim}0$ region (towards the particle side of the plateau).

Fractional QHE $\nu = 8/3$

The $\nu = 8/3$ is a fragile state in the second LL. The order is believed to be identical to the Particle-Hole conjugated $\nu = 2/3$ (on top of a full LL). For this state, we didn't make a thorough study of κ_{xx} along the plateau. We did measure κ_{xx} in the center, finding again a finite value $\kappa_{xx} = 0.41 \pm 0.03$ (see Fig. S3c), similar to the $\nu = 5/2$ state.

Further study of $\nu = 2$

We carefully studied the $\nu = 2$ state, concentrating on the magnetic fields where κ_{xx} becomes finite (Fig. S2c). Very interesting is the difference in slope $\partial\kappa_{xx}/\partial B$, which is significantly larger on the particle side (compared to the hole side). This could be attributed to the microscopic realization of the disorder, as the puddles that form when the second LL is slightly filled (when $\nu > 2$) are geometrically different from the hole puddles that form when the first LL is not completely full ($\nu < 2$).

Raw data

All the power measurements, which were fitted to extract κ_{xx} are presented in Fig. S3.

Noise acquisition and calibration

The noise arriving to the amplifier contacts (A_S and A_{PM}) is separately amplified by homemade cryo-amplifiers located on the 4.2K plate of the dilution refrigerator. The amplifier's input is connected (in parallel) to the sample resistance, the line capacitance, and a superconducting coil, forming an RLC circuit. In our system the central frequency of the circuit was 632kHz (695kHz) and the bandwidth was 42kHz (44kHz) for A_S (A_{PM}). The amplified noise is further amplified by a room temperature amplifier, and is measured with an SRS-865A lock-in amplifier.

The gain of the cryo-amplifiers was calibrated using equilibrium Johnson-Nyquist (JN) noise[2, 3]. The total measured voltage noise could be written as,

$$S_V = A^2\big(S_{\text{base}} + S_{\text{JN}}\big), \tag{S11}$$

with S_{base} being the base electronic noise of the amplifier circuit, A the gain, and S_{JN} the JN noise,

$$S_{\text{JN}} = 4k_b TR. \tag{S12}$$

With $R = G_{xy}^{-1}$ and T_0 the base electronic temperature. For high enough temperatures (above 30mK), the electronic temperature is well coupled to the cryostat's temperature $T_C = T_0$. Thus, measuring the equilibrium noise against T_C allows the calibration of the amplification gain, A and the base noise, S_{base} (Fig. 4). When the cryostat is cooled to the lowest temperatures (below 20mK), the electronic temperature can be larger than that of the cryostat. Here we the calibration of S_{base} to deduce the temperature,

$$T_0 = \frac{S_V - S_{\text{base}}/A^2}{4k_b R}. \tag{S13}$$

a

b

c

d

e
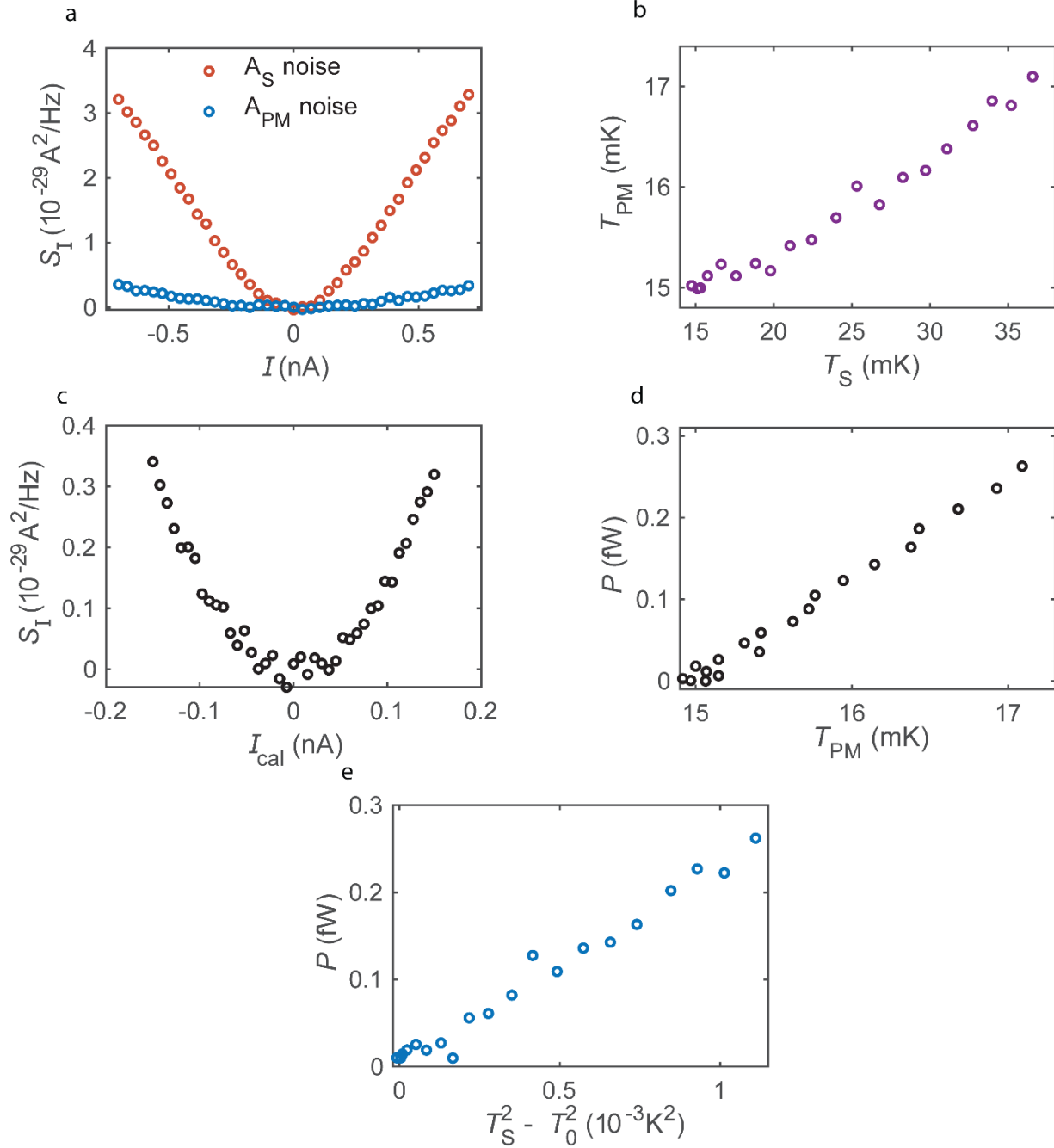
Fig. S1 – Methodology of power measurement. Measurement and analysis steps required to measure the heat flow, and extract κ_{xx}. As an example, we present $\nu = 2$ data, measured at $B = 6.1$T, and base temperature of $T_0 = 15$mK. **(a)** Raw noise data. The excess noise measured at A_S and A_{PM} as a function of the sourced current I sourced from S_1 (while current $-I$ is simultaneously sourced from S_2). **(b)** Power-meter's temperature as a function of the source's temperature extracted from **(a)** using Eq. S7. The heating of the source from $T_0 = 15$mk to a temperature of $T_S \sim 40$mK causes the slight increase of the PM's temperature to $T_{PM} \sim 17$mK, due to the finite κ_{xx}. **(c)** Power-meter calibration; raw data. Noise measured at A_{PM} as a function of the direct heating of the PM, by current I_{cal} sourced from S_1^{cal} (while

current $-I_{\text{cal}}$ is simultaneously sourced from S_2^{cal}). **(d)** Dissipated power (derived from Eq. S9) as a function of T_{PM}. **(e)** By combining the main measurement **(b)** with the calibration **(d)**, we can plot the power arriving to the PM as a function of the source temperature, and produce the plot presented in the main text Fig. 2a. A linear fit to the power vs. T_S^2 gives κ_{xx}.
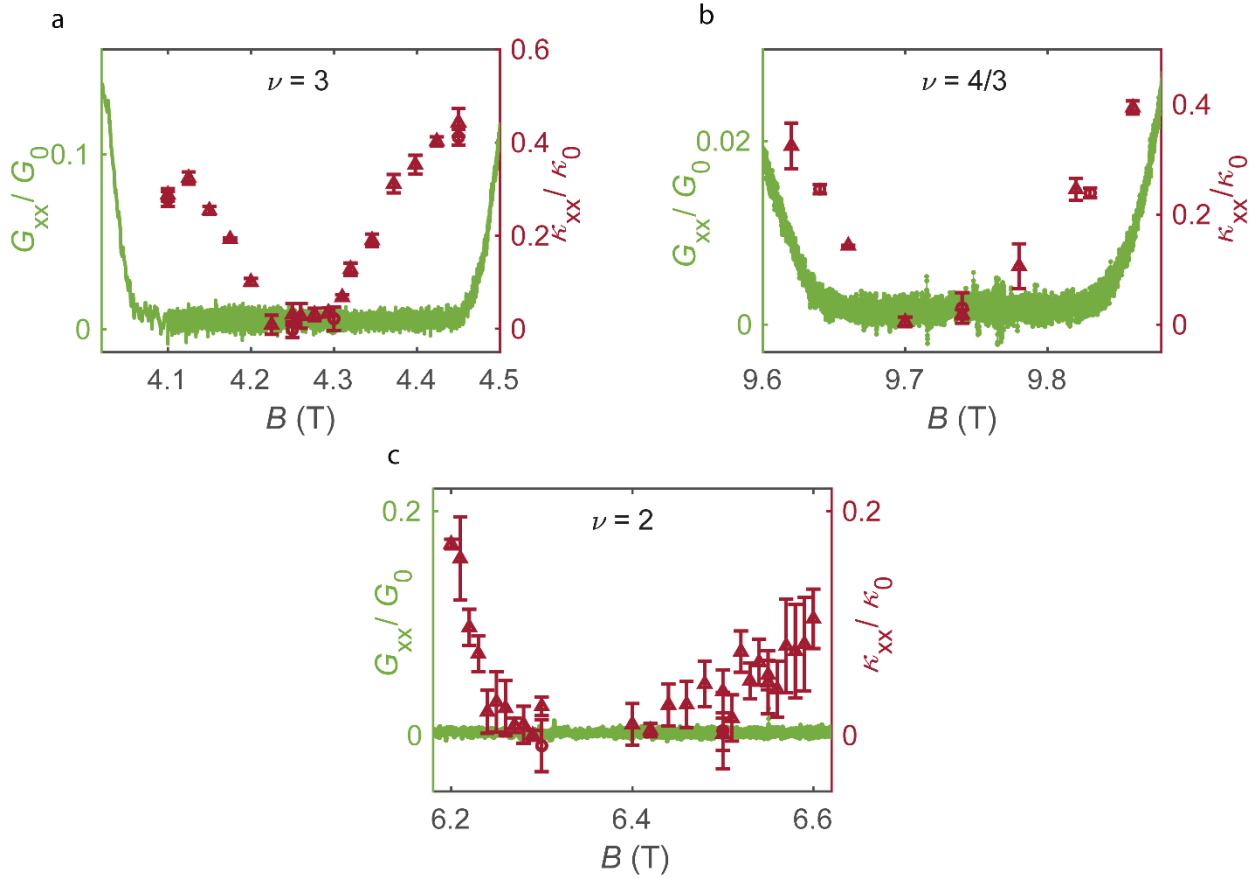

Fig. S2 – Thermal conductance through the bulk of other QHE states. Longitudinal electrical conductance (green with scale to the left) and longitudinal thermal conductance (red markers with scale on the right) plotted as a function of magnetic field on the plateaus of **(a)** $\nu = 3$, **(b)** $\nu = 4/3$ and **(c)** $\nu = 2$. The circular markers corresponds to the fitting results of P vs. T_S^2 (raw data presented in Fig. S3), and the triangular markers correspond to κ_{xx} measured for a single source temperature of $T_S = 50\text{mK}$, and extracted according to Eq. S10.
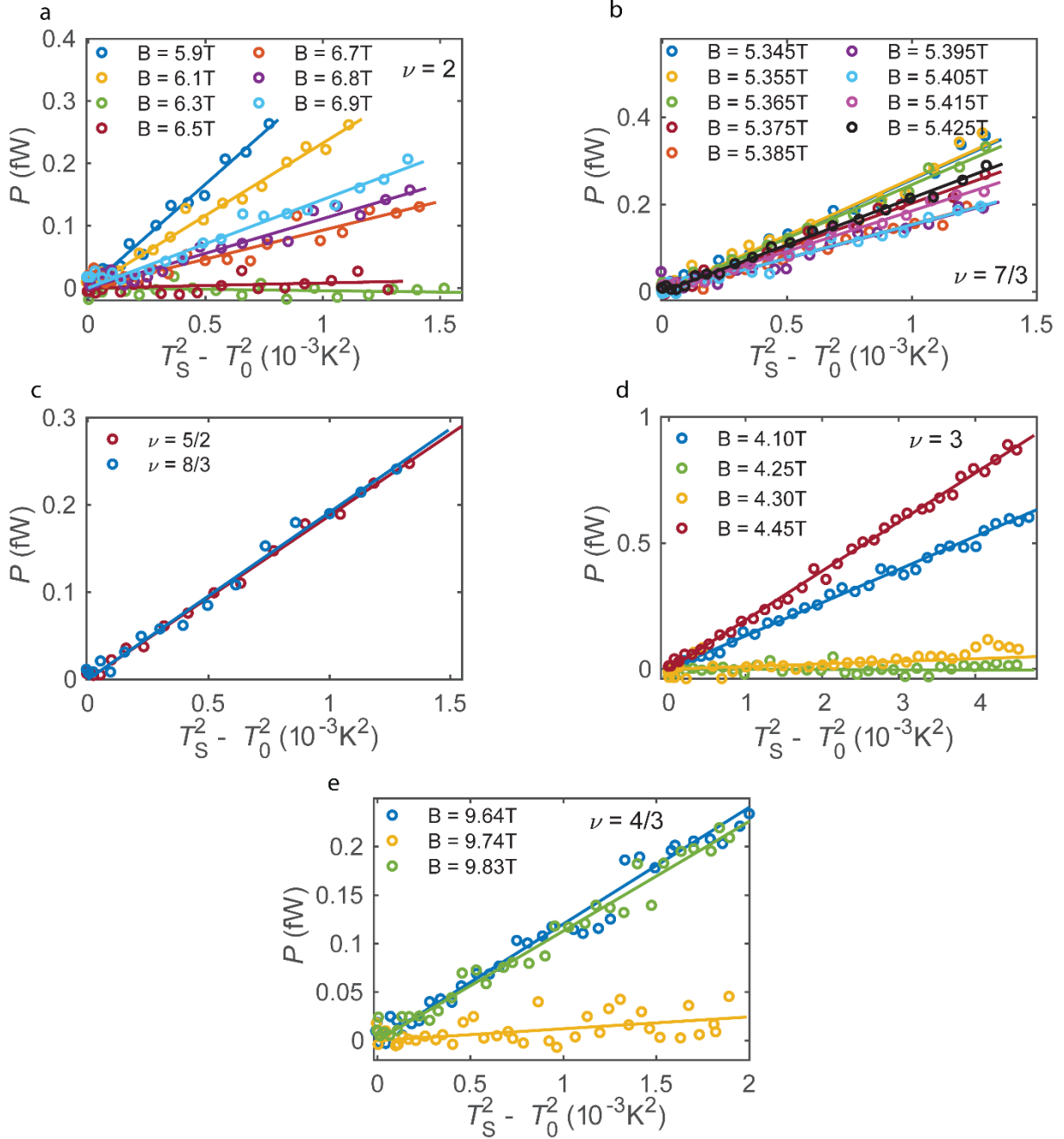
Fig.3 – Raw data used to extract κ_{xx}. The colored markers represent the power arriving to the PM as a function of the source temperature squared. The data is linearly fitted (colored straight lines) in order to extract κ_{xx} (according to Eq. 1 of the main text). Showing the measured data for the results appearing in the main text and the supplementary information: **(a)** $\nu = 2$, **(b)** $\nu = 7/3$, **(c)**, $\nu = 5/2$ and $\nu = 8/3$, **(d)** $\nu = 3$ and **(e)** $\nu = 4/3$.
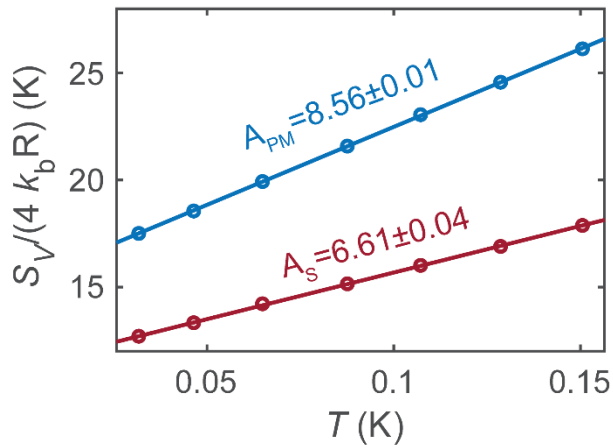
Fig. S4 – Amplifier calibration. Equilibrium noise as a function of the cryostat temperature (markers). The noise is linear in temperature, in agreement with the Johnson-Nyquist formula (Eq. S12). This allows us to calibrate the gain according to Eq. S13 (straight lines).

references

1. Jezouin S, Parmentier FD, Anthore A, Gennser U, Cavanna A, Jin Y, *et al.* Quantum limit of heat flow across a single electronic channel. *Science* 2013, **342**(6158)**:** 601-604.

2. Johnson JB. Thermal Agitation of Electricity in Conductors. *Physical Review* 1928, **32**(1)**:** 97-109.

3. Nyquist H. Thermal Agitation of Electric Charge in Conductors. *Physical Review* 1928, **32**(1)**:** 110-113.